Charged-Particle Tracking for Neutron-Deuteron Breakup

by

Kimberly K. Boddy

Submitted to the Department of Physics
in partial fulfillment of the requirements for the degree of

Bachelor of Science

at the

MASSACHUSETTS INSTITUTE OF TECHNOLOGY

June 2007

Author .....
Department of Physics
May 11, 2007

Certified by .....
Professor June L. Matthews
Department of Physics
Thesis Supervisor

Accepted by .....
Professor David E. Pritchard
Senior Thesis Coordinator, Department of Physics

Charged-Particle Tracking for Neutron-Deuteron Breakup

by

Kimberly K. Boddy

Submitted to the Department of Physics
on May 11, 2007, in partial fulfillment of the
requirements for the degree of
Bachelor of Science

Abstract

Particle tracking software has been developed to measure the energy of protons scattered in the breakup process $d(n, np)n$. The nd breakup experiment is performed at the Weapons Neutron Research facilities at Los Alamos Neutron Science Center. In order to fully define breakup kinematics for the stationary deuterium target, the following are measured: incident neutron beam energy, scattered proton energy and angle, and one of the scattered neutron angles. The proton energy is determined using a permanent magnet spectrometer, consisting of two permanent magnets placed between two wire chamber detectors. A particle tracking code uses the particle hit positions in the wire chambers to determine the proton's curvature (and hence deduce its energy) as it passes through the magnetic field of the magnets. Monte Carlo simulations show that the kinetic energy resolution is better at lower proton energies, when the magnetic field bends the particle more. The ultimate goal of the experiment is to measure the five-fold differential cross section to look for effects of three-nucleon forces.

Thesis Supervisor: June L. Matthews
Title: Professor of Physics

Acknowledgments

I would first like to thank Prof. June Matthews for allowing me this great experience of being a member of her research group and for all of her support and advice throughout these three years. Thank you to Taylan Akdoğan, who has shown me infinite patience and understanding; I am forever grateful for all that he has taught me and for all he has inspired me to learn. To Bill Franklin for the support he gave to me while I was at Bates and while I was preparing for DNP meetings. To Max Chtangeev for his kindness and generosity.

Thanks to Dan for the fun-filled physics times. Thanks to Tim for being Tim. And finally, thank you to my family, who have always believed in me.

Contents

List of Figures

List of Tables

Chapter 1

Introduction

Particle spectrometers are used to measure the energies of moving charged particles. They utilize a known magnetic field $\vec{B}(\vec{x})$ to bend the trajectories of the particles of charge q moving at velocity $\vec{v}$ as governed by the Lorentz force law

$$\vec{F} = q\left(\vec{v} \times \vec{B}(\vec{x})\right) \tag{1.1}$$

and from the detection of the particle, one can deduce its energy from its curvature. The detection system varies depending on the needs of the experiment. Spectrometers are often used to measure the energy of a final-state charged particle in scattering experiments, giving a potentially necessary parameter to describe the kinematics of an event.

Monte Carlo simulations are needed to reconstruct the trajectories of the particles; magnetic fields are not perfectly uniform, rendering analytical calculations of the particle energies infeasible. They are also particularly useful to reveal information about the spectrometer and the software that is used to analyze data from the spectrometer. For example, simulations determine the energy resolution of the spectrometer, which is essential for future error analysis. They also provide a test for the developed software, and it is the job of the experimentalist to ensure that energy resolution is not limited by poor event reconstructions.

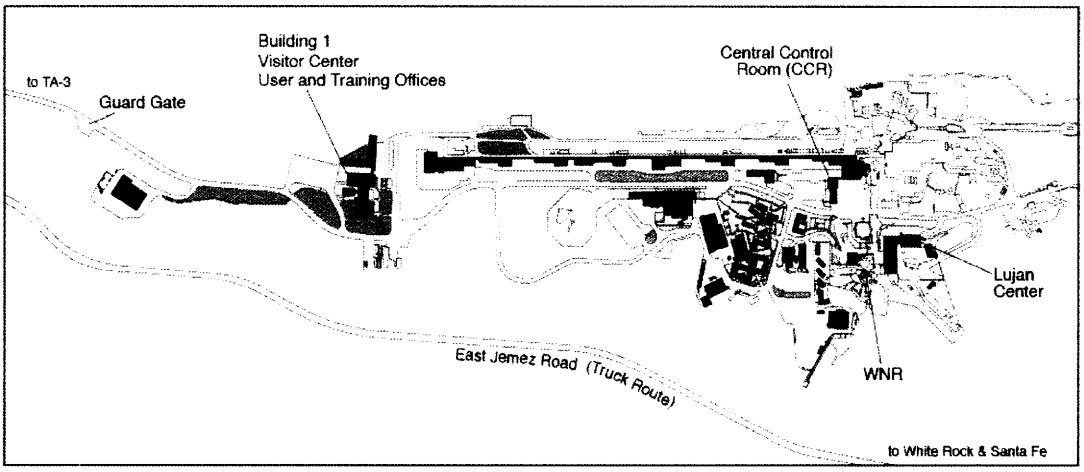

Figure 1-1: Map of TA-53.

1.1 Los Alamos National Laboratory

The Los Alamos National Laboratory (LANL) conducts numerous experiments, some of which focus on pure research. In specific, the Los Alamos Neutron Science Center (LANSCE) located in Technical-Area 53 (TA-53) of LANL allows non-LANL groups to come as users of the lab and perform experiments. The nuclear physics experiment described in Chapter 3 is carried out by an MIT-led collaboration, hosted by the LANSCE-NS group. Collaborators from MIT, the University of Kentucky, and Houghton College aim to study three-nucleon forces using the neutron beam provided by the Weapons Neutron Research (WNR) facility. The neutron beam is produced from an 800 MeV linearly accelerated proton beam, shown in Figure 1-1.

In order to study three-nucleon forces, the collaboration is measuring the five-fold differential cross section for neutron-induced deuteron breakup. An important aspect in the experiment is to know the energy of the scattered proton. A permanent magnet spectrometer is employed to detect the proton, and the author of this thesis has created a tracking code to regenerate event tracks of the protons and measure their energies. This thesis will present the theory and motivation of *nd* breakup and give an outline of the experiment as a whole. The spectrometer and tracking code will be described in detail, and results from a Monte Carlo simulation will be shown.

Chapter 2

Three-Body Interactions

Theoretical models for two-nucleon (NN) systems describe experimental data to a high degree of precision, popular NN potentials being AV18 [2], CD Bonn [3, 4], Nijm I, Nijm II, and Nijm 93 [5]. Measurements of observables for nucleon-nucleon scattering have been made for a wide range of energies and center-of-mass angles to give comprehensive databases[1], which complement the theoretical models. The case of three nucleons is quite different. Expansions of the two-nucleon models fail to describe systems with more than two nucleons. An example is that the predictions of the binding energies of ^{3}He and ^{3}H underestimate the experimental values by 1 MeV to 1.5 MeV. The current solution to correct the theory is to modify the nuclear Hamiltonian to include a three-nucleon force [1].

2.1 Three-Nucleon Forces

Presently accepted theoretical models describe the three-nucleon force (3NF) as a double pion exchange, and the Fujita-Miyazawa 3NF [6] adds an intermediate Δ excitation of the nucleus. A Feynman diagram of this representation is shown in Figure 2-1. The models that have been used the most frequently for current few-body calculations are the Urbana IX [7] and Tucson-Melbourne (TM) [8] 3NF's. More

[1]Such online databases for both experimental data and theoretical predictions include the Data Analysis Center from the Center for Nuclear Studies, NN-OnLine from the Radboud University Nijmegen, and Inversion OnLine from the University of Hamburg.

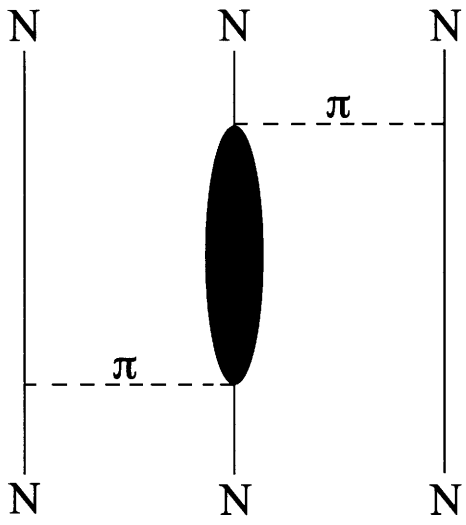

Figure 2-1: Feynman diagram of a 2π exchange with an intermediate Δ excitation to describe the 3NF.

recently, the TM model has been replaced by the Tucson-Melbourne prime (TM') model, which modifies the TM 3NF to be more consistent with chiral symmetry [9, 10].

2.2 Nucleon-Deuteron Breakup

J. Kuroś-Żolnierczuk has made a detailed theoretical study of three-nucleon breakup, focusing on nucleon-deuteron breakup [1]. She concludes that the most sensitive observables to 3NF's are the five-fold differential cross section and the A_{xx}, A_{yy}, and A_{xz} components of the tensor analyzing power. Also, 3NF effects in general increase with increasing incoming beam energy[2]. Comparing the different 3NF models, predictions using Urbana IX with AV18 and TM' with CD Bonn are close to each other for the differential cross section and for the analyzing powers and tensor analyzing powers, but TM with any NN potential provide distinctly different results. The TM + NN potential often gives much larger effects of 3NF's for the above observables than the Urbana IX + AV18 and TM' + CD Bonn potentials give.

Figure 2-2 shows two-dimensional projections onto phase space of the relative

[2]The study was made with beam energies of 13, 65, 135, and 200 MeV.

contribution $\Delta\sigma$ of the 3NF effects to the total breakup cross section:

$$\Delta\sigma_i = \left| \frac{\sigma_i^{(2N)} - \sigma_i^{(2N+\mathrm{TM})}}{\sigma_{\mathrm{tot}}^{(2N)}} \right| \times 100\% \tag{2.1}$$

where $\sigma_i = \sigma_{\mathrm{tot}}^{\mathrm{breakup}}$. These specific projections are for an energy of 135 MeV. The three columns show projections onto the planes $\theta_1 - \theta_2$, $\theta_1 - \phi_{12}$, and $E_1 - E_2$, where $\phi_{12} \equiv \phi_1 - \phi_2$ and θ is the center-of-mass (CM) angle. The first row shows results with no restrictions. The effects that are not experimentally accessible should not be included, so the second row is plotted with a σ cut, showing only those phase space points that give a cross section of $\sigma^{(2N)} \geq 0.01$ mb/sr^2 MeV for at least 5 MeV. Another demand is that the energies of the detected nucleons must be greater than 15 MeV for kinematical reasons, and the third row is plotted with the $\sigma + E$ cut. A particularly promising configuration to observe 3NF effects is at $\theta_1 \approx 15°$, $\theta_2 \approx 15°$, and $\phi_{12} \approx 0$. The scattered particle energy range should be 40 MeV to 70 MeV.

2.3 Breakup Kinematics

The specific three-body breakup reaction $n + d \rightarrow n + n + p$ will be relevant to the experiment presented in the next chapter. Using 4-momentum vectors, the kinematics of the neutron-induced deuteron breakup can be determined. The basic 4-momentum conservation equation is

$$\mathrm{P}_n^\nu + \mathrm{P}_d^\nu = \mathrm{P}_1^\nu + \mathrm{P}_2^\nu + \mathrm{P}_p^\nu \tag{2.2}$$

with the incoming neutron and target deuteron on the left-hand side of the equation and the resulting two neutrons and proton on the right-hand side. $\vec{p}_d = 0$ since the target is stationary and thermal motion of the target atoms average to zero. The incident neutron beam energy E_n and the scattered proton energy E_p are known, and the scattering angles of the proton θ_p and one of the neutrons θ_1 can be experimentally measured. The energies of the final-product neutrons E_1 and E_2 and the angle of the other scattered neutron θ_2 can be determined. Following the method by T. Akdoğan

[11] and setting $c = 1$, define

$$\begin{aligned} \mathrm{P}^\nu &\equiv \mathrm{P}^\nu_n + \mathrm{P}^\nu_d - \mathrm{P}^\nu_p & p_x &= p_n - p_p \sin\theta_p \\ \mathrm{P}^\nu &= (E, \vec{p}) & p_y &= p_n - p_p \cos\theta_p \\ E &= E_n + E_d - E_p & \theta &= \tan^{-1}\tfrac{p_y}{p_x} \\ \vec{p} &= \vec{p}_n - \vec{p}_p & M^2 &= E^2 - (p_x^2 + p_y^2). \end{aligned} \tag{2.3}$$

Rearranging Equation 2.2 and squaring both sides yields

$$\begin{aligned} [\mathrm{P}^\nu_2 = \mathrm{P}^\nu - \mathrm{P}^\nu_1]^2 \\ m_n^2 = M^2 + m_n^2 - 2(EE_1 - \vec{p}\cdot\vec{p_1}) \\ EE_1 - pp_1\cos(\theta - \theta_1) = \frac{M^2}{2} \\ EE_1 - Bp_1 = A \\ (EE_1 - A)^2 = B^2(E_1^2 - m_n^2) \\ E_1^2(E^2 - B^2) + E_1(-2AE) + (A^2 + m_n^2 B^2) = 0 \end{aligned}$$

where $A \equiv \frac{M^2}{2}$ and $B \equiv p\cos(\theta - \theta_1)$. Solving the quadratic equation,

$$E_1 = \frac{EA \pm \sqrt{E^2A^2 - (E^2 - B^2)(A^2 + B^2 m_n^2)}}{E^2 - B^2}. \tag{2.4}$$

By energy conservation, $E_2 = E - E_1$. The angle θ_2 is determined by taking another arrangement of Equation 2.2 and squaring both sides:

$$\begin{aligned} [\mathrm{P}^\nu - \mathrm{P}^\nu_2 = \mathrm{P}^\nu_1]^2 \\ M^2 + m_n^2 - 2(EE_2 - pp_2\cos(\theta - \theta_2)) = m_n^2 \\ \cos(\theta - \theta_2) = \frac{2EE_2 - M^2}{2pp_2} \\ \theta_2 = \theta - \cos^{-1}\left(\frac{2EE_2 - M^2}{2pp_2}\right). \end{aligned} \tag{2.5}$$

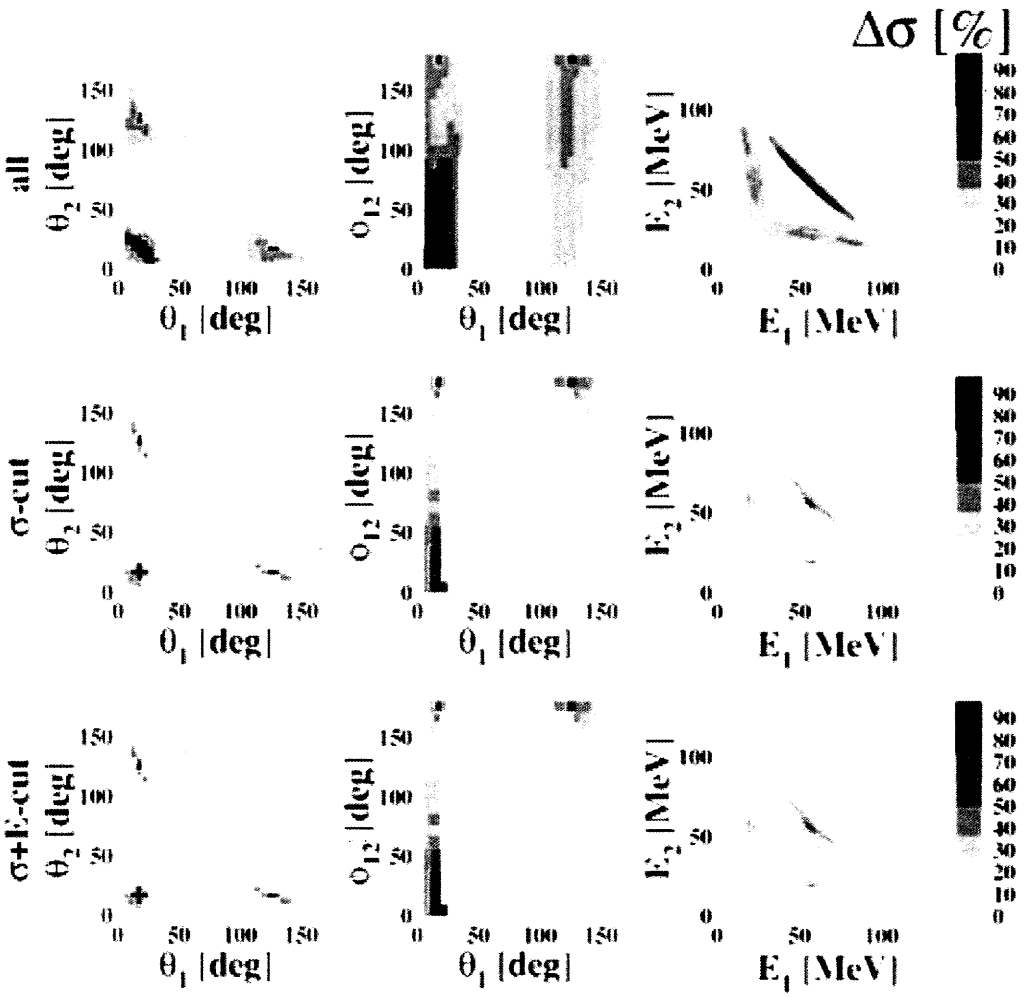

Figure 2-2: Projections of $\Delta\sigma$ onto the planes $\theta_1 - \theta_2$, $\theta_1 - \phi_{12}$, and $E_1 - E_2$ for no cuts, σ cuts, and $\sigma + E$ cuts. Figure from ref. [1].

Chapter 3

Neutron-Deuteron Breakup at LANL

3.1 Facilities

An MIT-led collaboration is running an experiment to study 3NF's at the Los Alamos National Laboratory (LANL) in Los Alamos, New Mexico. The Los Alamos Neutron Science Center (LANSCE) has a mile-long linear accelerator to produce an 800 MeV unpolarized proton beam, which is then directed towards Target-4, an unmoderated tungsten spallation source, to produce pulsed neutron beams for the Weapons Neutron Research facility. The resulting beams are white neutron beams, allowing for a continuum of energies ranging from about 0.1 MeV to 800 MeV. The energy of the neutrons can be determined from time-of-flight information, which is available due to the known flight path lengths and pulsed nature of the beams. Under normal operating conditions, there are 120 macropulses per second, spaced 625 μs apart. Within each macropulse are 0.2 ns micropulses, spaced 1.8 μs apart. The long time between the short micropulses ensures that micropulses of varying energies do not overlap [12].

Once the proton beam hits Target-4, neutron beams are made at different angles as shown in Figure 3-2. The names of the various flight paths for the collimated neutron beams indicate which target they originate from and how many degrees they are away from the incident proton beam. The experimental area for *nd* scattering is

located on 4FP15R, 15° to the right of the incoming proton beam.

Due to quasi-free spin-orbit interactions between the protons and tungsten nuclei, there is an induced polarization in the resulting neutron beams. The measured polarization [13, 14] of the 4FP15R neutron beam is shown in Figure 3-1.

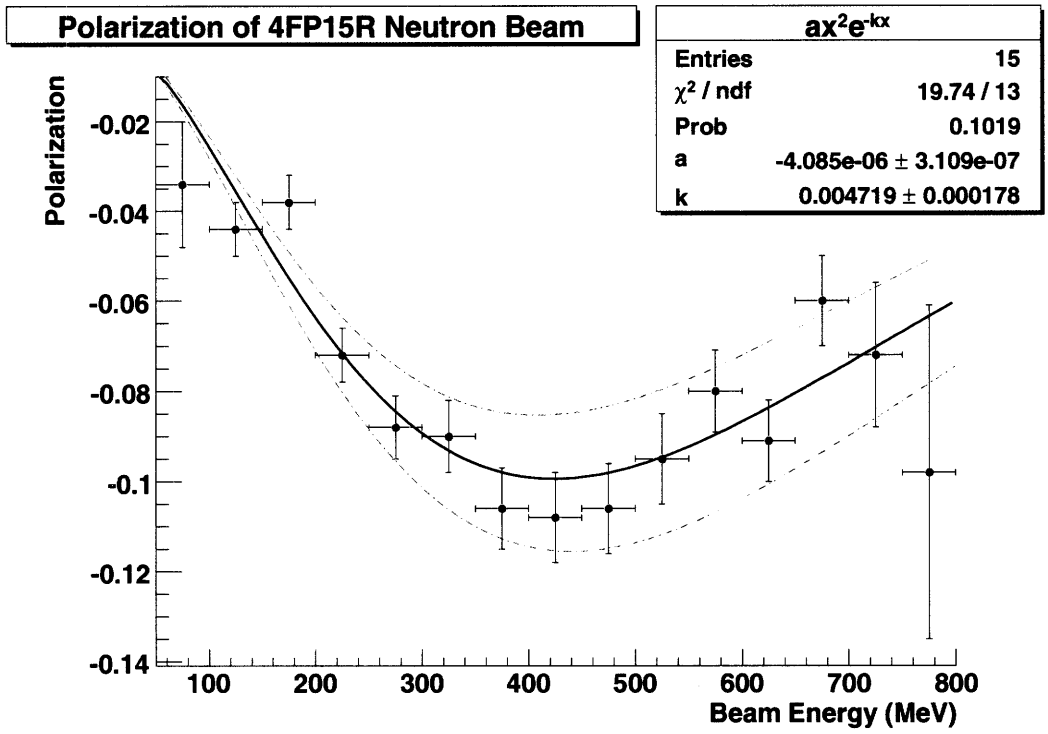

Figure 3-1: Neutron beam polarization on 4FP15R as a function of beam energy. The solid line is the exponential fit ax^2e^{-ikx}, while the dashed lines represent the extrema of the fitted parameters.

3.2 Experimental Setup

Figure 3-3 shows a schematic representation of the detector layout. The beam enters the room and first encounters a fission chamber to measure the flux of incident neutrons by measuring the yield of neutron-induced fission of ^{238}U. More information regarding the chamber can be found in ref. [15]. The beam then hits a liquid deuterium target. Any unscattered neutrons are discarded in the beam dump outside the room. As indicated in Figure 3-3, the z axis is defined to be along the direction of the beam, the y axis points from the ground towards the ceiling of the room, and

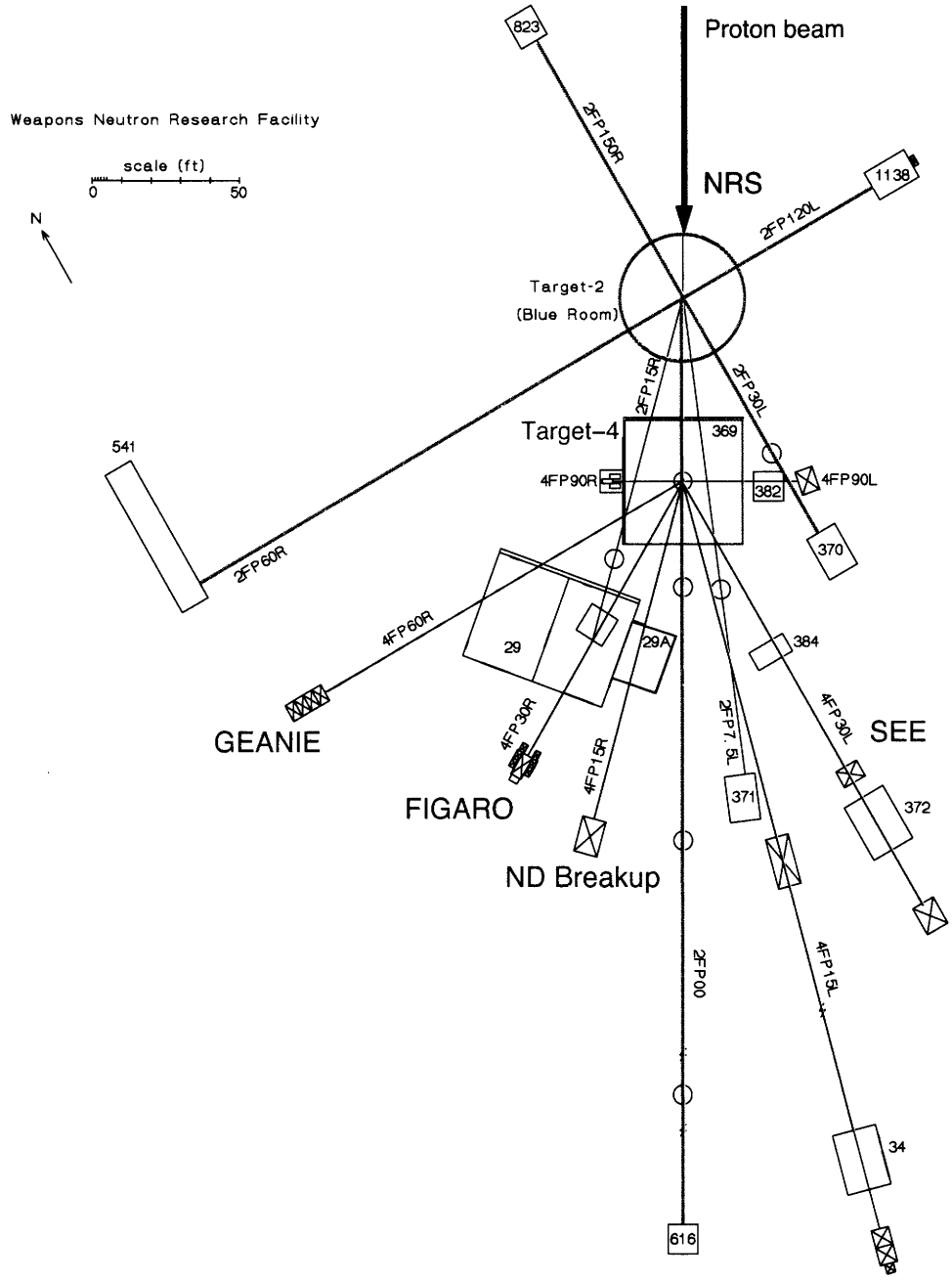

Figure 3-2: Layout of the Weapons Neutron Facility. Flight paths in green show the beams created from Target-2; paths in blue show the neutron beams created from Target-4, a tungsten spallation source. The *nd* breakup experiment is situated on 4FP15R.

the x axis is positioned such that the coordinate system is right-handed. The origin is located at the center of the target.

3.2.1 Target

The target container is a cylindrical flask 3" in diameter. The cylindrical surface is made with a 2 mm thick mylar window, and the end caps of the cylinder are made of 6.5 mm thick pieces of stainless steel. The target is placed with its cylindrical axis vertical, perpendicular to the beam, to reduce background due to double scattering from the steel covers [11]. The flask is sealed in a cylinder-shaped scattering chamber 32 cm in diameter. The body of the chamber is made of $\frac{3}{16}$" stainless steel with a 5 mm thick kapton window spanning 180° of the cylinder.

3.2.2 Proton Detection

A permanent magnet spectrometer is employed to determine the momentum of scattered protons. Two permanent magnets and two wire chambers are centered at beam height, 49", and at an angle of 17° to the right of the beam. This position is ideal to look for 3NF's, as shown in the theoretical prediction in Figure 2-2.

The magnets are positioned with their magnetic fields pointing upwards in the $+y$ direction so that the positively charged particles bend away from the beam. The maximum magnetic field of either magnet reaches $\sim$ 3000 G. There is a ΔE detector placed directly in front of the wire chamber closest to the target, and there is an E detector placed directly in back of the wire chamber farthest from the target. The ΔE and E scintillators are used for timing and particle identification. Each is attached to a photomultiplier tube (PMT), which is supplied a high voltage (HV) of about -2000 V and sends an amplified signal to a data room when a particle is detected. Details about the wire chambers follow in § 3.3.

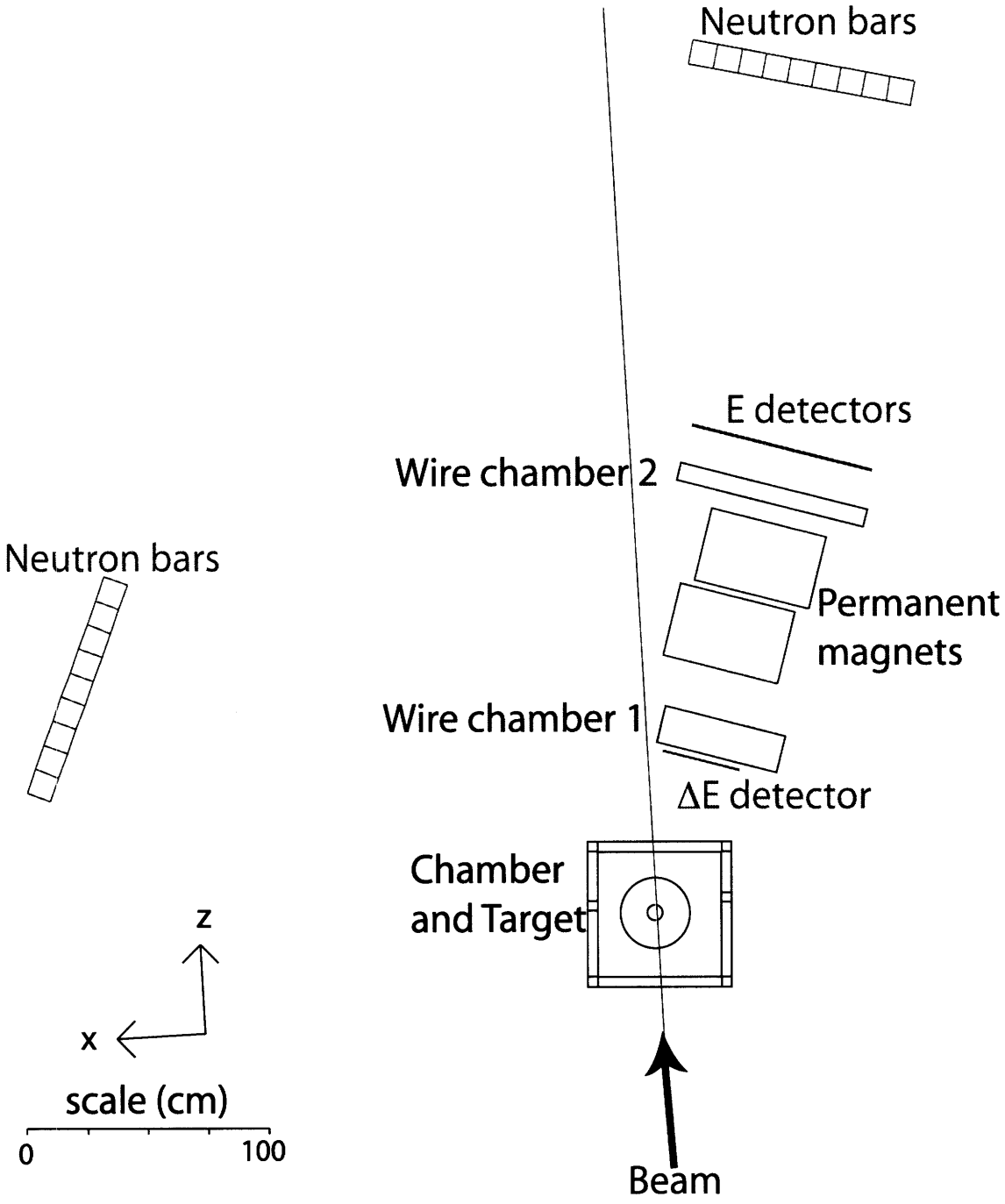

Figure 3-3: Layout of the detectors.

3.2.3 Neutron Detection

Neutrons are detected by neutron walls each made of nine neutron scintillation bars. The bars are 10 cm $\times$ 10 cm $\times$ 200 cm and are place near-vertically, side-by-side. A metal pin is inserted into a drilled hole on one end of the bar to support the bar in a metal stand. There are PMT's attached to both ends of the bars, and they operate at about -2000 V. Based on the time difference between the signals created by a neutron to reach each end of a bar, the vertical y position of the particle can be calculated. The x position is determined from which bars are hit.

One neutron wall is centered at a far forward angle of 14° to the right of the beam, farther away from the target than the spectrometer as not to block scattered protons and to give good time-of-flight resolution. The position of this wall is consistent with looking for nd breakup where two scattered particles come out at small forward angles on the same side of the beam. The other neutron wall is centered at 67° to the left of the beam. This location will allow a simultaneous measurement of quasifree np scattering in the deuterium as a consistency check. Due to physical restrictions regarding where the wall can be placed, only the last four bars at the largest angles can be used to make this measurement.

3.3 Permanent Magnet Spectrometer

Two permanent magnets provided by LANL are used to bend the positively charged particles away from beam line. The frames are shaped like hollowed-out boxes with two open ends, and they have inhomogenous magnetic fields due to the spacing between the SmCo bar magnets placed on the top and bottom of the inside of the frames. Graphs of the normal field component (y direction) are shown in fig. 3-4. The origins for these graphs are located at the centers of the respective magnets. The z direction in this figure indicates the direction along the open ended length of the magnet.

The wire chambers consist of 0.48 cm thick adjacent Al planes. There are four planes to detect the trajectory of a particle; two sets of orthogonal planes per wire

chamber serve to determine two x and y positions of the particle. These anode planes have either vertical (to determine the x position) or horizontal (to determine the y position) 20 μm gold-plated tungsten wires spaced 8 mm apart wound into the anode frame. The anode wires are directly coupled into a fast delay line with two anode outputs for each plane. There are also 76 μm gold-plated copper-clad aluminum cathode wires spaced 8 mm apart interlaced between the anode wires. The odd (even) cathode wires are bussed together so as to provide two cathode outputs for each plane. There are 6.3 μm thick mylar foils aluminized on both sides that are epoxied to the planes to provide a ground plane between the anode planes [16]. The Al planes have an entrance window cut into them to expose only the wires and mylar foils for particle detection. Schematic drawings of the wire chambers are in Figure 3-5 and Figure 3-6. The front wire chamber (closer to the target) is labeled WC1, and the back wire chamber (farther away from the target) is labeled WC2. The four planes in each wire chamber with anode wires are labeled X1, Y1, X2, and Y2, starting from front plate with the BNC connectors going towards the back plate. Anode wires are located on the side of the anode plane that is farther away from the front plate of the wire chamber. The front plates of both WC1 and WC2 face towards the target. There might, however, be a discrepancy in the locations of the anode planes as indicated. Mechanical drawings of the wire chambers were not found, and the wire chambers were built too long ago for the designers to remember. The anode plane position presented is the most likely configuration based on educated guesses, and

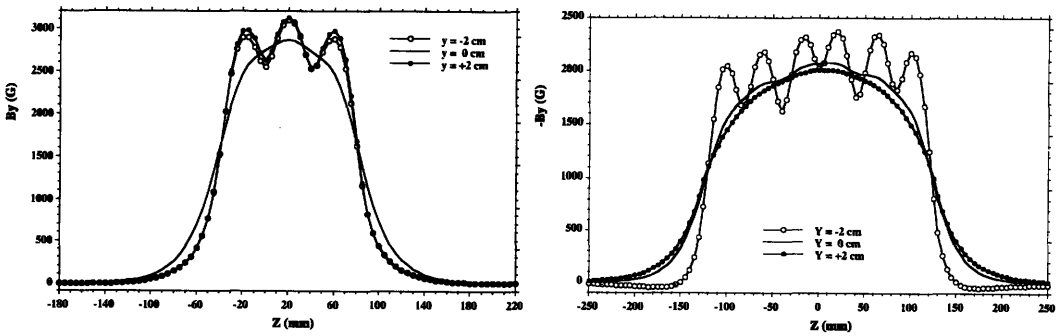

(a) PM1 (b) PM2

Figure 3-4: Normal field components of the permanent magnets.

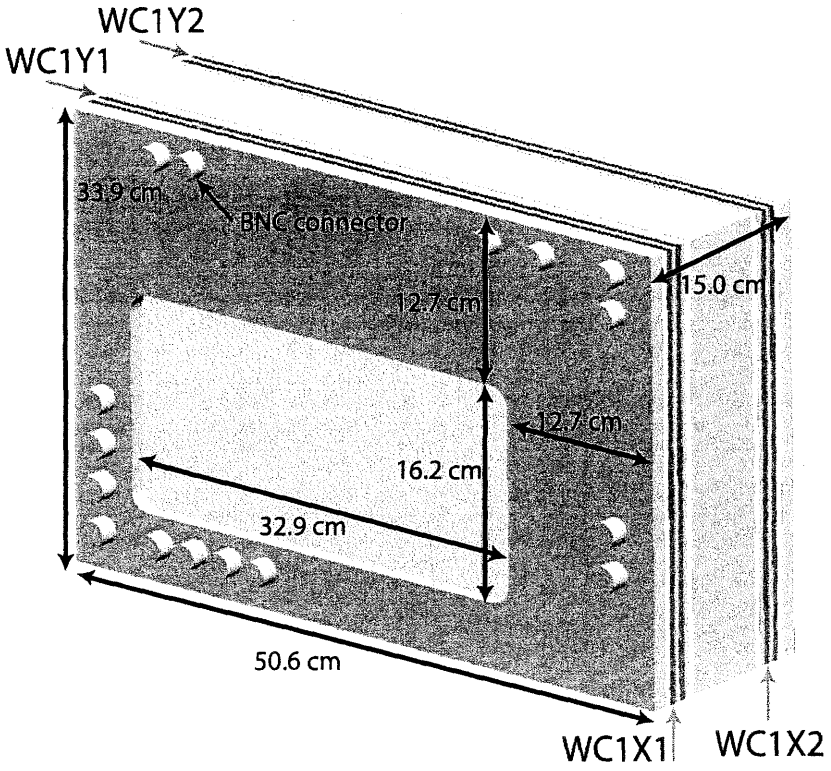

Figure 3-5: Schematic drawing of WC1. The dimensions of the frame and mylar windows are shown. Anode planes are labeled and colored in red. The BNC connectors shown on the face of the connector plate are not drawn to scale. All other planes are either spacer planes or ground planes.

certain knowledge of the plane positions most likely cannot be determined without destroying the detector by disassembling it.

The anode planes run at around an HV of +2000 V. A gas mixture of 65% Ar and 35% isobutane flows through the wire chambers. As a charged particle passes through the window of the wire chamber, it ionizes the gas, which then creates a signal for the closest anode to carry to the two ends of the delay line. Using the times t_1 and t_2 taken for the signal to reach the ends of the delay line, the drift distance of the particle from the anode wire can be calculated and the position at which the particle hit the detector can be determined with a resolution of $\sigma = 125$ μm.

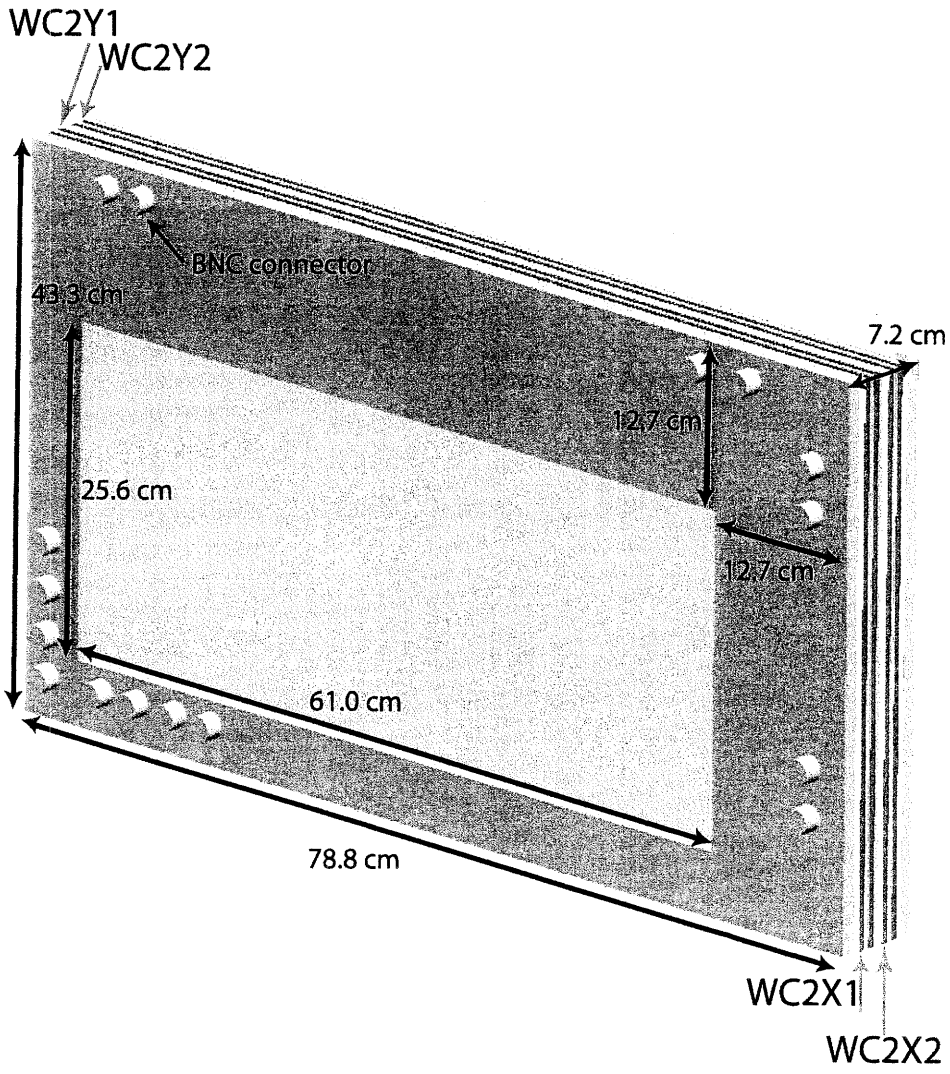

Figure 3-6: Schematic drawing of WC2. See Figure 3-5 for details.

3.4 Wire Chamber Calibration

The wire chamber calibration is performed as described in ref. [16].The time-to-digital converter (TDC) times t_1 and t_2 are used to determine the positions of the anodes for the nearest particle position x. If the time difference is defined as

$$t_d = t_2 - t_1, \tag{3.1}$$

then the particle position is

$$x = a_0 + a_1 t_d + a_2 t_d^2 \tag{3.2}$$

where the quadratic term accounts for dispersion in the delay line. Then, define

$$k = \mathrm{Int}(x/w)w \tag{3.3}$$

where w is the anode wire spacing (8 mm for the chambers described in § 3.3) and Int is a function that truncates its argument to the nearest integer. The constants a_0, a_1, and a_2 are found by minimizing the chi-square function

$$\chi^2 = \sum_{i=1}^{n} (x_i - k_i)^2 \tag{3.4}$$

for n particles.

To find the relationship between drift time and drift distance, consider the time sum

$$t_s = t_1 + t_2 + (\text{path length corrections}). \tag{3.5}$$

The path length corrections can be ignored if the scintillator defining the TDC start time is near the wire chambers. Notice that t_s is independent of x and is equal to twice the drift time plus any path length corrections. Assuming that, on average, the drift cells are uniformly illuminated (which is possible for the small drift cell size of 8 mm), then the distribution of particles in time ($\mathrm{d}N/\mathrm{d}t$) is related to the distribution

of particles in space $(\mathrm{d}N/\mathrm{d}s) = c$:

$$\frac{\mathrm{d}N}{\mathrm{d}t} = \frac{\mathrm{d}N}{\mathrm{d}s}\frac{\mathrm{d}s}{\mathrm{d}t} = cv(t) \tag{3.6}$$

where $v(t)$ is the drift velocity $(\mathrm{d}s/\mathrm{d}t)$. The drift distance $s(t)$ is then found by integrating over drift time:

$$s(t) = \frac{1}{c}\int_0^t \left(\frac{\mathrm{d}N}{\mathrm{d}t}\right)\mathrm{d}t. \tag{3.7}$$

The issue of whether to add or subtract the drift distance from the anode position (i.e., which side of the anode the particle passed by) can be clarified using two different approaches. The first requires multiple anode planes, four vertical and four horizontal planes, to completely specify a particle trajectory of two positions and two angles. Since the wire chambers used in the *nd* experiment do not have eight anode planes per wire chamber, the other method needs to be used. More information for the multiple anode plane method can be found in ref. [16].

The second method to resolve the left-right ambiguity is to use the induced cathode pulses. Odd/Even boxes constructed at the University of Kentucky are voltage-sensitive differential amplifiers that can generate the difference between the two signals per plane that are bussed together. The odd (even) wires create a positive (negative) signal for particles passing to one side of the anode wire, and a negative (positive) signal for particles passing to the other side.

3.5 Detector Efficiencies

In order to calculate the efficiencies of each of the eight planes in the two wire chambers, data were taken with a CH_2 target but without the magnets. In analyzing a single plane, the total number of hits is counted as all the events in the calibration runs for which all the other planes detect the events. The good hits are those for which the plane detects the events along with all the other planes. In the case of any event in which one of the other planes does not detect the event, the event is

discarded for the plane being analyzed and does not count against the efficiency of the plane. The efficiency then is the ratio of the number of good hits to the total number of hits.

In some cases, the particle hits the wire chamber at such an angle as to not go through all of the planes. These cases should not be used to count against the plane efficiencies, so position acceptance cuts are made to reject these tracks. Calibration runs were taken at varying HV values around -2000 V. The resulting efficiencies for the planes of WC1 and WC2 are shown in Figure 3-7 and Figure 3-8, respectively.

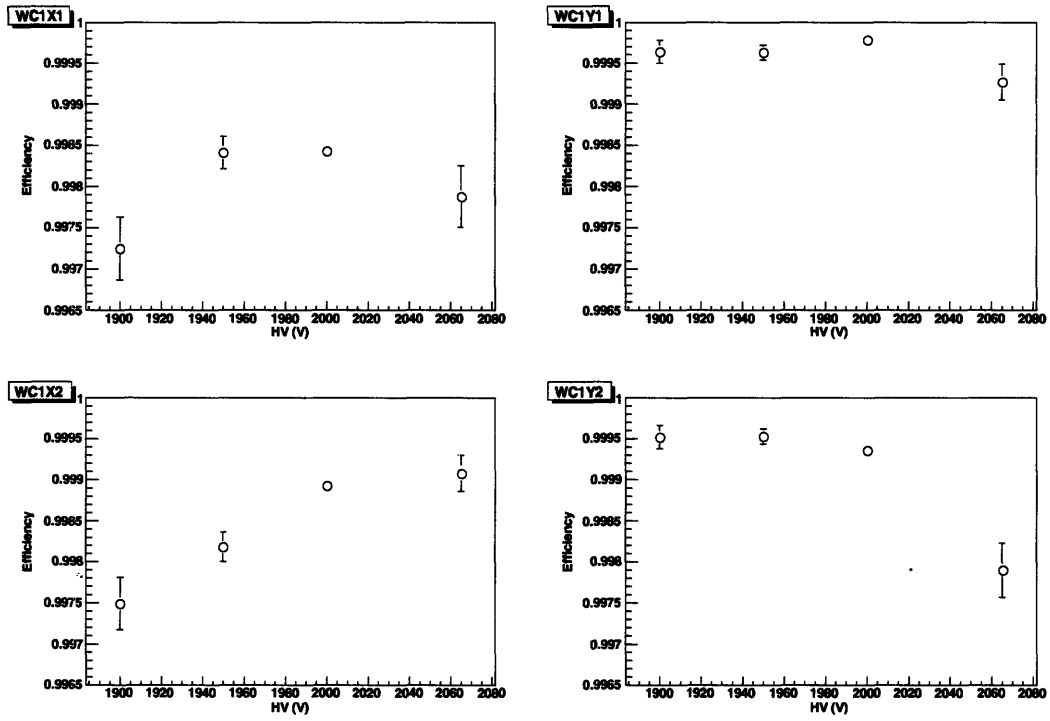

Figure 3-7: Efficiencies for the planes of WC1.

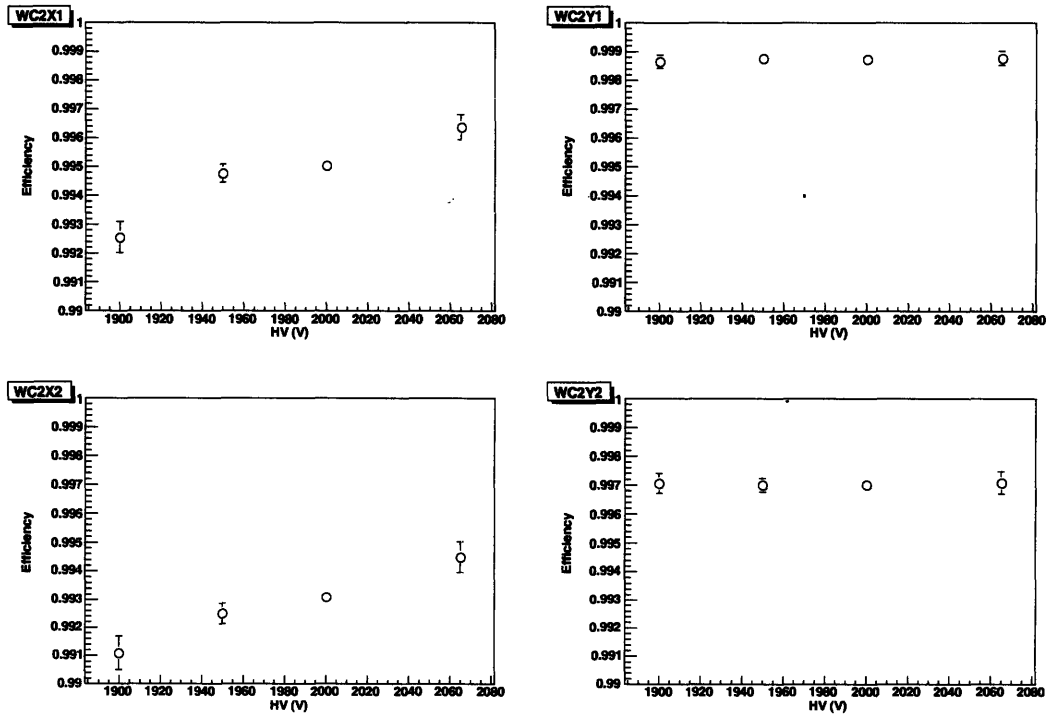

Figure 3-8: Efficiencies for the planes of WC2.

Chapter 4

Monte Carlo Simulation

A C++ Monte Carlo simulation has been built with the assistance of T. Akdoğan to determine the kinetic energy of a charged particle passing through the magnetic spectrometer. The code creates a truth event by specifying the incoming energy and direction of a proton and stores the positions where the proton hits the wire chamber planes. These hit points are fed back into the code to determine the best fit energy and direction. Comparing many truth events to the corresponding reconstructed events at various energies determines the resolution of the spectrometer.

4.1 Charged Particle Tracking

Given the wire chamber hit positions, the code makes an initial guess by taking the points approximately defined by (WC1X1, WC1Y1) and (WC1X2, WC1Y2) (it is only an approximation since the X and Y planes do not overlap each other) and defining the angles θ and ϕ. θ is the angle of inclination in the x direction away from the beam (z axis), and ϕ is the angle of inclination in the y direction away from the beam. The hit positions on WC1 determines the straight line the particle takes before entering the magnetic field and, hence, determines the line on which the origin of interaction lies, as the breakup interaction may occur anywhere inside the target. The code "swims" the particle from the origin, through WC1, through the magnetic field, and finally through WC2. Straight lines can be used for all motion

outside of the range of the magnets, but swimming the particle through the magnetic field uses the Runge-Kutta method as described in § 4.1.1. Additionally, the initial guess takes the angles it has calculated and makes a search through 80 values for the initial momentum between 100 MeV/c and 700 MeV/c with a finer search for the lower momenta. The initial momentum is that which gives the best fit to the truth event. The code then makes a more in-depth search for the best fit using the Newton-Raphson method described in § 4.1.2.

In order to determine what the best fit is, calculations of χ^2 are used. The difference in the truth hit positions and the ones found via reconstruction gives a χ_i^2 value for the i^{th} anode plane. Since there is an uncertainty $\sigma = 125$ μm in determining the position of the anode wire, a normal pseudo-random number generator chooses values between $-\sigma$ and σ to add to the positions of the truth hits, and the reconstruction fits to those modified hit positions. The overall reduced χ^2 for the eight anode planes of WC1 and WC2 is

$$\chi^2/\text{dof} = \sum_{i=1}^{8} \left(\alpha_i^{\text{truth}} - \alpha_i^{\text{recon}}\right)^2 / (\sigma^2 \times 3) \tag{4.1}$$

where α_i is the appropriate x or y hit value on the i^{th} anode plane for the truth and reconstructed events and the factor of 3 represents the number of degrees of freedom. The goal is to determine the best starting position, initial energy, and initial direction that gives the smallest reduced χ^2, which will be referred to simply as χ^2 for the remainder of the chapter. The Newton-Raphson method varies the adjustable parameters (i.e., initial position coordinates x and y, initial momentum P, and angles θ and ϕ) to find the minimal χ^2.

4.1.1 Runge-Kutta Method

In order to simulate the charged particle swimming through the magnetic field, the magnetic field is interpolated at the particle's location and the particles advances a step on the order of a few millimeters. The new location of the particle is used to repeat the process until the particle exits the magnetic field. The step size is adjusted

appropriately such that for instances where the particle's trajectory will curve more (due to small momentum and/or a strong magnetic field at the particle's particular location), the particle is limited to travel a shorter distance. Smaller step sizes in the areas affecting the particle the most will increase the accuracy of the trajectory.

Each point of the particle's trajectory through the magnetic field is determined using the fourth-order Runge-Kutta method as outlined in ref. [17]. The Runge-Kutta method is based on the Euler method, which says that a solution y_n is advanced from x_n to $x_{n+1} \equiv x_n + h$ by the formula

$$y_{n+1} = y_n + hf(x_n, y_n) \tag{4.2}$$

where $f(x, y(x)) = y'(x)$. From Taylor expanding y_{n+1}, the step's error is of order h^2, making this method first order. The Euler method is not very accurate compared to other higher-order methods nor is it particularly stable. The second-order Runge-Kutta method takes a trial step and uses the derivative information at the midpoint to determine the direction of the real step:

$$\begin{aligned} k_1 &= hf(x_n, y_n) \\ k_2 &= hf(x_n + \frac{h}{2}, y_n + \frac{k_1}{2}) \\ y_{n+1} &= y_n + k_2 + \mathcal{O}(h^3). \end{aligned} \tag{4.3}$$

Although accuracy does not necessarily increase with higher orders, the fourth-order Runge-Kutta method is considered to be superior to the second-order and is used more often than any other order [17]. It evaluates the derivative four times: at the

initial point, at two trial midpoints, and at a trial endpoint. The formulas are

$$\begin{aligned} k_1 &= hf(x_n, y_n) \\ k_2 &= hf(x_n + \frac{h}{2}, y_n + \frac{k_1}{2}) \\ k_3 &= hf(x_n + \frac{h}{2}, y_n + \frac{k_2}{2}) \\ k_4 &= hf(x_n + \frac{h}{2}, y_n + \frac{k_3}{2}) \\ y_{n+1} &= y_n + \frac{k_1}{6} + \frac{k_2}{3} + \frac{k_3}{3} + \frac{k_4}{6} + \mathcal{O}(h^5). \end{aligned} \tag{4.4}$$

These equations are used at each point that the particle's trajectory makes in the magnetic field. The amount by which the particle steps is pre-determined by the code and slightly adjusted depending on the curvature of the particle's path at a given point, as previously mentioned. The information needed is the momentum of the particle at its current location, which gives the direction it needs to move in for the next step. The derivative information in this case is proportional to the acceleration as determined by the Lorentz force law.

4.1.2 Newton-Raphson Method

Minimizing χ^2 with respect to the particle's initial position, momentum, and direction will yield the best fit reconstructed particle track; however, simply taking one such parameter and varying it over a specified interval to find the minimum χ^2 does not give the desired results. Since χ^2 is not a smooth function of these parameters, a code searching for a minimum can get easily stuck on one of the many local minima that exist. To avoid this problem, χ^2 is minimized using the Newton-Raphson method as outlined in ref. [17].

The Newton-Raphson method is a one-dimensional root-finding method. It uses the function $f(x)$ and its derivative $f'(x)$. Geometrically, the tangent point of $f(x = x_i)$ is extended until it crosses the x axis at $x = x_{i+1}$. The process is then repeated, taking the tangent point of $f(x = x_{i+1})$ until the root is found or found within a

given acceptance range. Using a Taylor expansion,

$$f(x+\delta) = f(x) + f'(x)\delta + \frac{1}{2}f''(x)\delta^2 + \cdots . \tag{4.5}$$

Terms that are quadratic and higher will be insignificant and can be dropped for small enough δ if the functions are well-behaved. The root occurs when $f(x+\delta) = 0$, giving

$$\delta = -\frac{f(x)}{f'(x)}. \tag{4.6}$$

For $\delta = x_{i+1} - x_i$, the Newton-Raphson formula becomes

$$x_{i+1} = x_i - \frac{f(x)}{f'(x)}. \tag{4.7}$$

If the initial guess is far from the root, then higher-order terms beyond linear are important and the Newton-Raphson formula fails and can give inaccurate and meaningless results. For this reason, the initial guess procedure outlined at the beginning § 4.1 is particularly important and needs to give a result close to the result from the truth event. The Newton-Raphson method is then used to find the minimum χ^2 by finding the root of its derivative with respect to x, y, P, θ, and ϕ individually. Minimizing with respect to z is unnecessary since the angles act a substitute with regard to degrees of freedom. For instance, the derivative with respect to P is calculated as

$$\frac{\mathrm{d}\chi^2}{\mathrm{d}P} = \frac{\chi^2(P+\delta P) - \chi^2(P)}{\delta P} \tag{4.8}$$

where δP must be declared by the user of the code and the dependence of χ^2 on the other parameters has been suppressed for brevity. The double derivative (the $f'(x)$ term in Equation 4.7) is calculated as

$$\frac{\mathrm{d}^2\chi^2}{\mathrm{d}P^2} = \frac{[\chi^2(P+2\cdot\delta P) - \chi^2(P+\delta P)] - [\chi^2(P+\delta P) - \chi^2(P)]}{(\delta P)^2}. \tag{4.9}$$

Then, δP should change to be

$$\delta P = -\frac{(\mathrm{d}\chi^2/\mathrm{d}P)}{(\mathrm{d}^2\chi^2/\mathrm{d}P^2)}. \tag{4.10}$$

The same process occurs repeatedly for all the parameters until certain conditions on χ^2 and on the change in parameters are satisfied.

4.1.3 Particle Energy Loss

The charged particle loses energy traversing air, the wire chamber windows (mylar), the scattering chamber window (kapton), the target flask (mylar) and part of the target itself, assuming the interaction did not occur on the very edge of the target. The energy loss should be taken into account to properly reconstruct real physics events once the Monte Carlo is implemented into the data analyzer at a later date. Unfortunately, the results presented in § 4.2 do not include the energy losses, but a brief description of the attempt to implement the losses follows.

Stopping powers for protons as functions of energy through various materials are obtained from the NIST PSTAR database [18]. The PSTAR program, however, does not have the option of calculating the stopping power of protons in liquid deuterium. Following M. Chtangeev's treatment for particle energy loss in the CSDA (Constant Slowing Down Approximation) range [12], the stopping power (mean rate of energy loss) is given by the Bethe-Bloch equation

$$-\frac{\mathrm{d}E}{\mathrm{d}x} = Kz^2\frac{Z}{A}\frac{1}{\beta^2}\left[\frac{1}{2}\ln\frac{2m_ec^2\beta^2\gamma^2T_{\max}}{I^2} - \beta^2 - \frac{\delta}{2}\right] \tag{4.11}$$

where the variables are given in Table 4.1. T_{max} is the maximum kinetic energy that can be given to a free electron in a single collision:

$$T_{\max} = \frac{2m_ec^2\beta^2\gamma^2}{1 + 2\gamma m_e/M + (m_e/M)^2}. \tag{4.12}$$

Symbol	Definition	Units or Value
M	Incident particle mass	MeV/c^2
E	Incident particle energy γMc^2	MeV
T	Kinetic energy	MeV
$m_e c^2$	Electron mass $\times$ c^2	0.510 999 06(15) MeV
r_e	Classical electron radius $e^2/4\pi\epsilon_0 m_e c^2$	2.817 940 92(38) fm
N_A	Avogadro's number	6.022 136 7(36) $\times$ 10^{23} mol^{-1}
ze	Charge of incident particle	
Z	Atomic number of medium	
A	Atomic mass of medium	
K/A	$4\pi N_A r_e^2 m_e c^2/A$	0.307 075 MeV g^{-1} cm^2 for $A = 1$ g mol^{-1}
I	Mean excitation energy	eV
δ	Density effect correction to ionization energy loss	

Table 4.1: Variables used in the Bethe-Bloch equation. β and γ have their usual kinematical meanings.

The distance traveled by the particle with initial energy E in the medium is

$$R = -\int_E^0 \frac{\mathrm{d}x}{\mathrm{d}E'}\,\mathrm{d}E'. \tag{4.13}$$

The density effect correction δ can be ignored for the proton energy range of the experiment.

It is clear based on geometry how much mylar and kapton the particle traverses when passing through the target, scattering chamber, and wire chamber windows and how much air it traverses (recall that the target is vacuum-sealed in a scattering chamber, so the particle does not encounter air until after it exits the chamber). From the hit points on WC1, the origin of interaction can be determined as lying on a line that traces back through the target (since the target is of finite volume and not merely a point target), so the exact point of interaction cannot be known. Using an average, however, the origin of interaction should be taken as the midpoint of the line that traces through the target. Half the length of that line can be used as the distance the particle traverses the target.

4.2 Kinetic Energy Resolution

The resulting track reconstruction is pictorially shown in Figure 4-1. The code is used as a Monte Carlo to find the resolution for the spectrometer. The resolution is determined by creating 1000 truth events for a single kinetic energy T. For each truth event, the initial position and direction are chosen by a pseudo-random generator. There are restrictions on θ and ϕ due to the angular acceptance of the spectrometer, the limiting factor being the magnets. The range of the angles depend on the origin of interaction in the target and on the energy of the particle, as particles with lower energies might curve outside the magnetic field before it reaches the far end of the field and could possibly run into the side of the magnet. Each of these truth events are fed back into the code to reconstruct the event. The resulting 1000 reconstructed event energies form a normal distribution around the kinetic energy of the truth event, giving a standard deviation σ_T that is interpreted as the spectrometer's error in determining the resolution at that particular energy.

Figures 4-2 and 4-3 show the energy distributions and their Gaussian fit statistics found using ROOT [19] for "true" kinetic energies of 10, 20, 35, 50, 75, 100, 125, 150, 175, and 200 MeV. Figure 4-4 uses the fit information from the distributions to determine the kinetic energy resolution and the error in the determining the kinetic energy. The resolution is

$$\rho = \frac{T_{\text{recon}} - T_{\text{truth}}}{T_{\text{truth}}} \tag{4.14}$$

while the relative error in the kinetic energy is

$$\epsilon_T = \frac{\sigma_T}{T}. \tag{4.15}$$

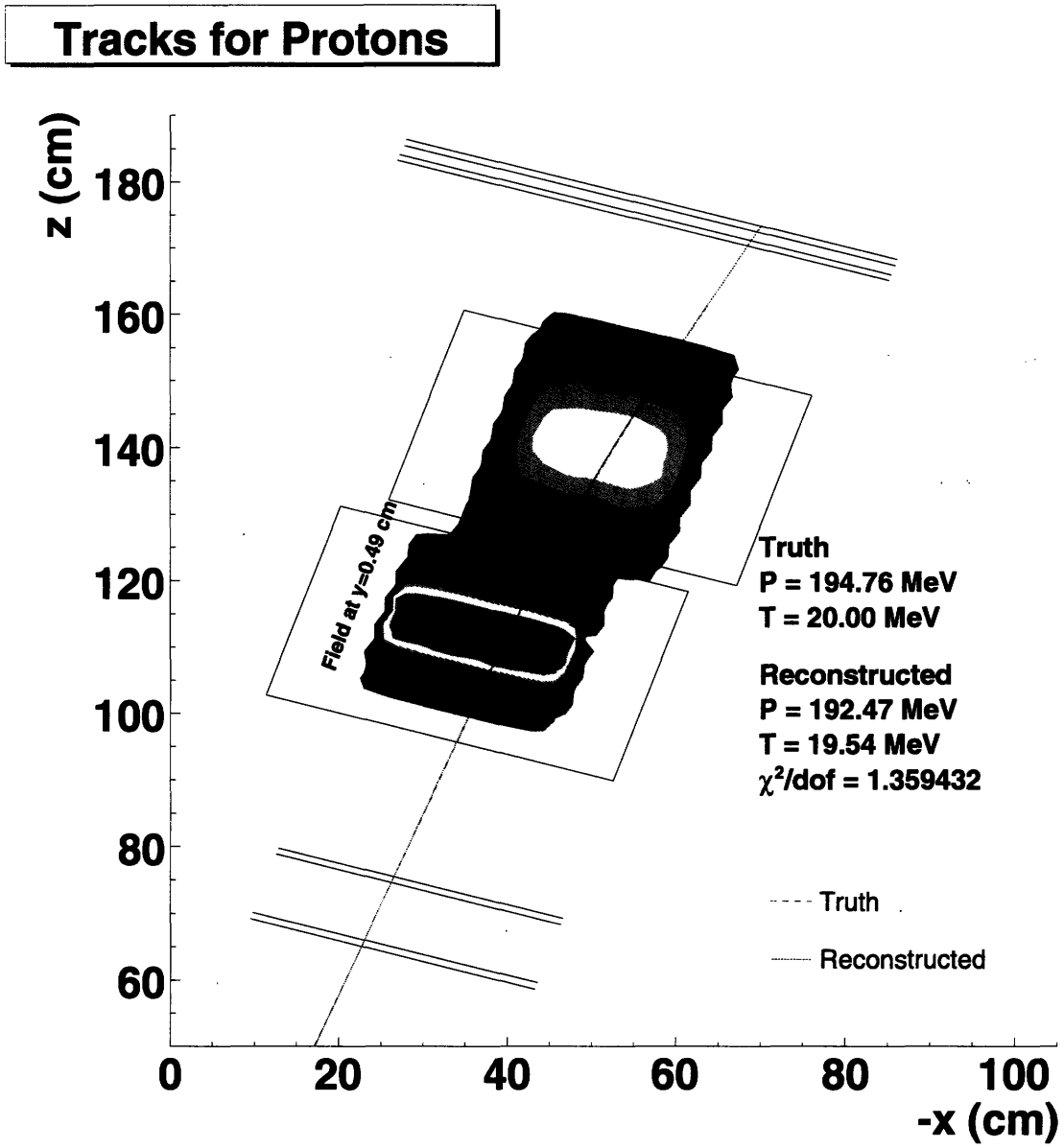

Figure 4-1: Sample track reconstruction for a proton of energy 20 MeV. Lines for the wire chamber anode planes (for the width of the wire chamber window) are drawn, as well as the outline of the inner wall of the permanent magnets, showing the physical restrictions of the tracks.

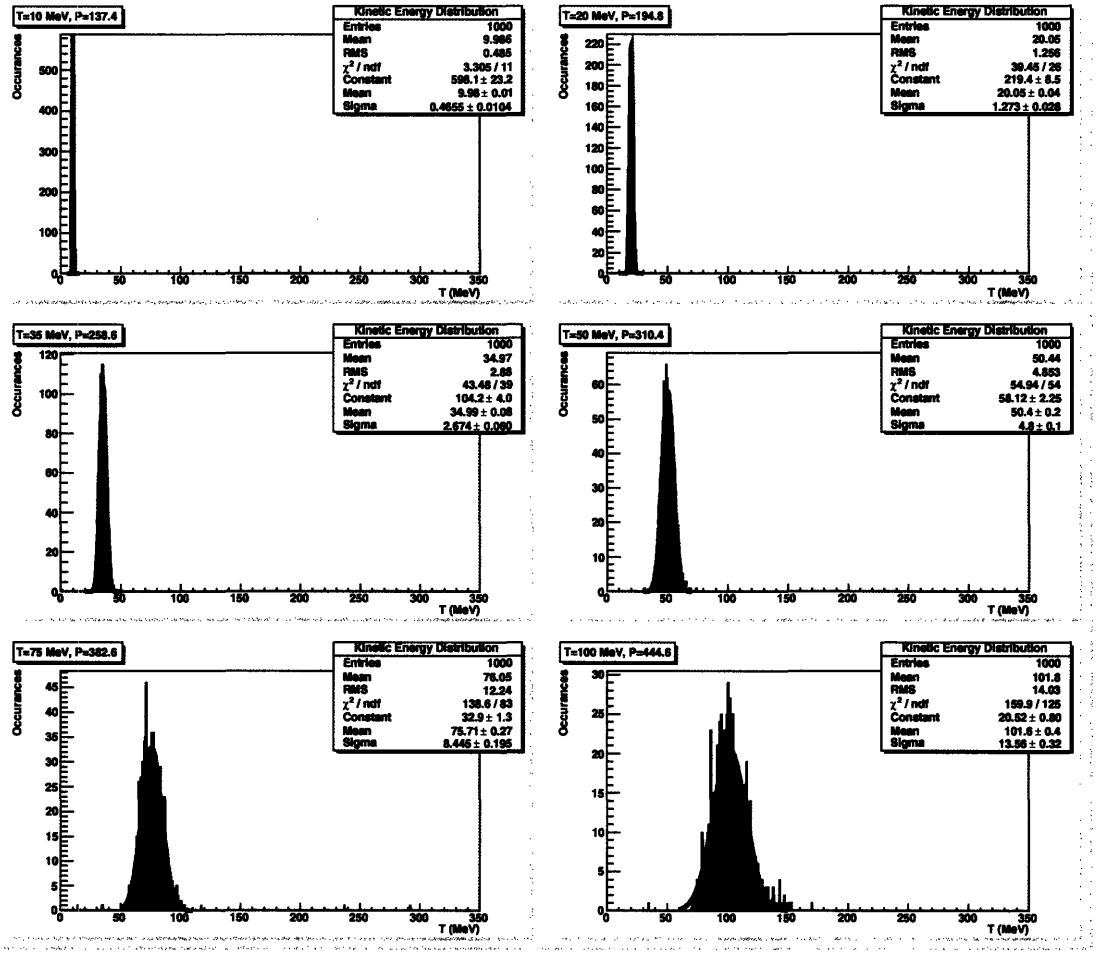

Figure 4-2: Kinetic energy distributions for energies of 10, 20, 35, 50 75, and 100 MeV.

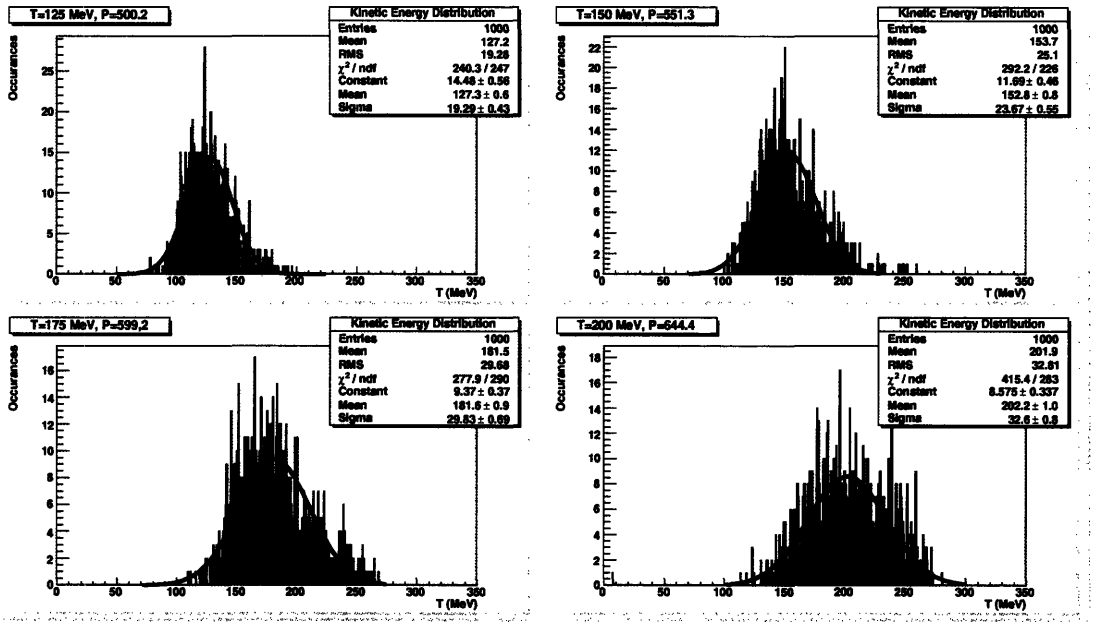

Figure 4-3: Kinetic energy distributions for energies of 125, 150, 175, and 200 MeV.

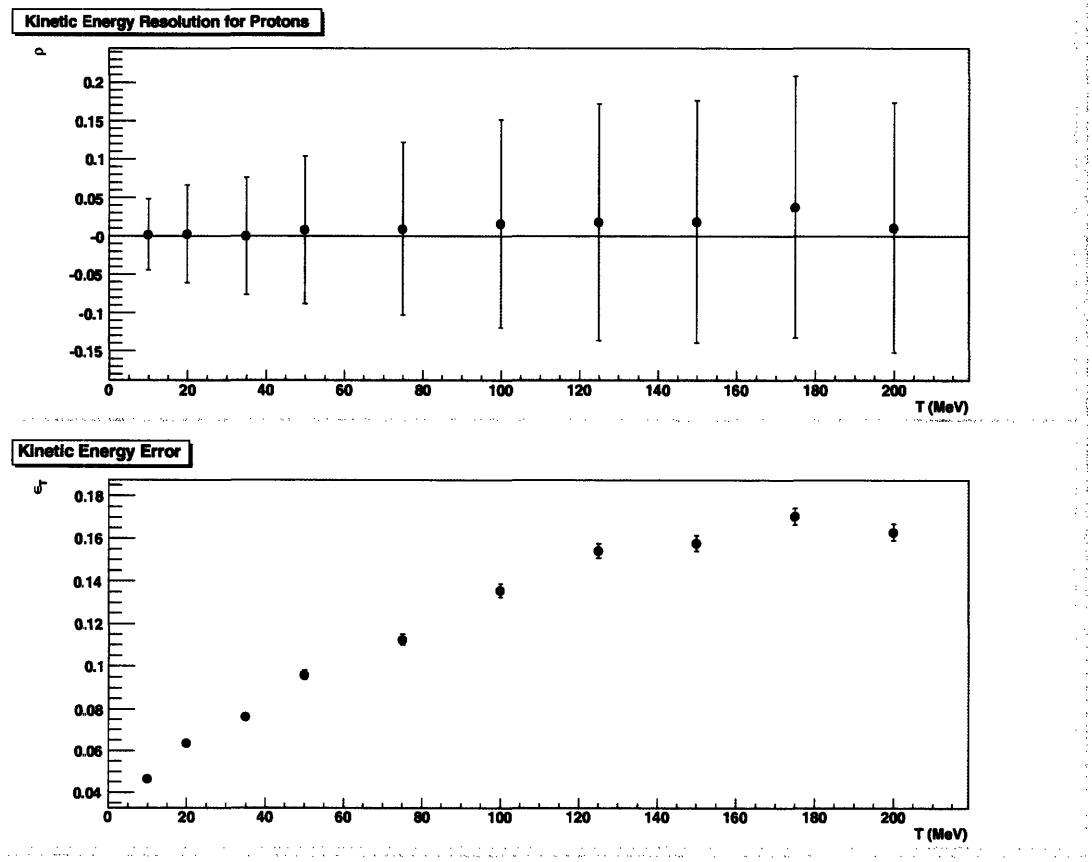

Figure 4-4: Kinetic energy resolution and error.

Chapter 5

Conclusions

Figure 4-4 shows an increase in the uncertainty in determining kinetic energy as the energy increases. This result is expected: high energy particles will have a nearly straight trajectory passing through the magnetic field, so it is difficult for the code to distinguish between a 150 MeV and 200 MeV particle. The resolution of the spectrometer is limited by the permanent magnets' small magnetic field size and strength. However, the important energies of the detected proton are in the range of 40 MeV to 70 MeV, from Figure 2-2. It is in this energy range where 3NF effects are predicted to be most prominent, and the spectrometer has an acceptable resolution of approximately 10% error in this range.

The next steps for the particle tracking code are to include particle energy losses for the proton traversing material and to implement the code into the data analyzer. Then, real TDC information can be used to reconstruct proton trajectories and energies in *nd* breakup. The health of the tracking code is heavily dependent on the magnetic field. It is possible to detect a particle that has managed to avoid the magnetic field in part or all together by passing along the inner edge of the magnet frame. Although these events would be physically possible, they should be cut from the analysis since the code would not be able to accurately reconstruct the event. Only particles that traverse the entire length of the magnetic field are used to determine the spectrometer resolution, and there should be some way of determining which data are usable with the tracking code. The code should also be optimized as

much as possible to allow it to run in real time with the rest of the data analyzing software, instead of having to reanalyze data offline. Apart from those issues, the tracking code is prepared for real breakup data.

Bibliography

[1] J. Kuroś-Żolnierczuk *et al.*, Phys. Rev. C **66** (2002).

[2] R. Wiringa, V. Stoks, and R. Schiavilla, Phys. Rev. C **51** (1995).

[3] R. Machleidt, F. Sammarruca, and Y. Song, Phys. Rev. C **53** (1996).

[4] R. Machleidt, Phys. Rev. C **63** (2001).

[5] V. Stoks, R. Klomp, C. Terheggen, and J. de Swart, Phys. Rev. C **49** (1994).

[6] J. Fujita and H. Miyazawa, Prog. Theor. Phys. **17** (1957).

[7] B. Pudliner, V. Pandharipande, J. Carlson, S. Pieper, and R. Wiringa, Phys. Rev. C **56** (1997).

[8] S.A. Coon *et al.*, Nucl. Phys. **A317** (1979).

[9] J. Friar, D. Hüber, and U. van Kolck, Phys. Rev. C **59** (1999).

[10] D. Hüber, J. Friar, A. Nogga, H. Witala, and U. van Kolck, Few-Body Syst. **30** (2001).

[11] T. Akdoğan, *Pion Production in the Neutron-Proton Interaction*, PhD dissertation, MIT, 2003.

[12] M. Chtangeev, Neutron-deuteron elastic scattering and the three-nucleon force, Master of science, MIT, 2005.

[13] K. Boddy *et al.*, Beam polarization correction for neutron-deuteron scattering cross section, Bulletin of the American Physical Society, 2005.

[14] J. Hough, Polarization of high energy neutrons in proton-nucleus scattering, Bachelor of science, MIT, 2001.

[15] S.A. Wender *et al.*, Nucl. Inst. Meth. **A336**, 226 (1993).

[16] C. Morris, NIM **196**, 263 (1982).

[17] W. H. Press, B. P. Flannery, S. A. Teukolsky, and W. T. Vetterling, *Numerical Recipes in C* (Cambridge University Press, 1992).

[18] National Institute of Standards and Technology, Stopping-Power and Range Tables for Protons, http://physics.nist.gov/PhysRefData/Star/Text/PSTAR.html, 2005.

[19] R. Brun *et al.*, ROOT, http://root.cern.ch, 2006.